

Research Article

Noble Metal Decoration and Presulfation on TiO₂: Increased Photocatalytic Activity and Efficient Esterification of *n*-Butanol with Citric Acid

Yu Niu,^{1,2} Pan Huang,^{1,3} Fuying Li,^{2,3} Kai Yang,³ Jinbei Yang,¹
Renzhang Wang,² Cheng Lin,¹ and Ting Qiu¹

¹School of Chemical Engineering, Fuzhou University, Fuzhou 350116, China

²Collaborative Innovation Center of Clean Coal Gasification Technology, Sanming University, Sanming 365004, China

³Research Institute of Photocatalysis, State Key Laboratory of Photocatalysis on Energy and Environment, Fuzhou University, Fuzhou 350002, China

Correspondence should be addressed to Ting Qiu; tingqiu@fzu.edu.cn

Received 5 January 2016; Accepted 11 February 2016

Academic Editor: Andrea Speltini

Copyright © 2016 Yu Niu et al. This is an open access article distributed under the Creative Commons Attribution License, which permits unrestricted use, distribution, and reproduction in any medium, provided the original work is properly cited.

TiO₂ has been widely used as a key catalyst in photocatalytic reactions; it also shows good catalytic activity for esterification reactions. Different sulfated M-TiO₂ nanoparticles (M = Ag, Au, Rh, and Pt) were prepared by photodeposition and ultrasonic methods. The results show that the noble metal nanoparticles, which were loaded onto a TiO₂ surface, slightly affected the crystal phase and particle size of TiO₂. Among all the catalysts, SO₄²⁻/Au-TiO₂ exhibited the best catalytic activity in the esterification reaction for the synthesis of citric acid *n*-butyl acetate and in the decomposition of methyl orange, as confirmed by a high conversion rate of up to 98.2% and 100% degradation rate, respectively. This can be attributed to an increase in the Lewis acidity of the catalyst and increased separation efficiency of electron-hole pairs. This superior catalyst has great potential applications in esterification reactions and wastewater treatments.

1. Introduction

TiO₂ has received much attention because of its superior photocatalytic activity, chemical stability, low cost, and non-toxicity [1–3]. However, pure TiO₂ is not effective for solar-driven applications. This can be achieved by the modification of semiconductors [4, 5], addition of transition metals [6], nonmetal doping [7–10], and use of coupled semiconductors. Several studies have been reported using noble metals as the cocatalysts for the decomposition of dyes [11–13]. The role of noble metals in the acceleration of dye degradation is twofold: (i) the injected electrons from TiO₂ are easily trapped by noble metals, thus achieving more efficient charge separation; (ii) noble metals are excellent catalysts for the reduction of O₂ because of easy activation and adsorption; they can absorb more low-energy visible light. The confined electrons on the surface of noble metal nanoparticles can be rapidly scavenged by O₂, thus avoiding the accumulation of

electrons on noble metals and also increasing the formation of superoxide radical anions [14].

Furthermore, acid-modified titania has great potential as a catalyst [15–18]. SO₄²⁻ modified TiO₂ solid acid nanoparticles exhibited better catalytic activity than pure TiO₂ nanomaterials, because of the coexistence of both Brønsted and Lewis acid sites and many other unique properties [19, 20]. In recent years, various studies have reported the extensive use of SO₄²⁻/TiO₂ solid acid catalyst, an environmentally friendly catalyst, in many catalytic reactions such as esterification and also in the efficient degradation of organic dyes [11, 12, 21]. For example, Wind et al. [22] used sulfated TiO₂ nanotubes as the catalyst for the esterification of acetic acid with cyclohexanol. It showed a high catalytic activity for acetic acid conversion, whereas anatase TiO₂ showed no catalytic activity. Muggli and Ding [12] reported that sulfated TiO₂ was more active and deactivated more slowly than

P-25 during the photocatalytic oxidation of acetaldehyde above 373 K. Sulfate doping has been shown to strengthen visible absorption, thus accelerating the degradation reactions [23].

Although esterification and degradation of organic dyes are seemingly very different, similar catalysts are used in both the reactions and widely used in various industries. Therefore, the utility and versatility of the $\text{SO}_4^{2-}/\text{M-TiO}_2$ catalysts can be verified by using these two very different types of reaction systems; relevant common factors can also be identified to help in the design and preparation of catalysts.

Based on the above considerations, in this study, Ag, Au, Rh, and Pt were selected as the model noble metals to modify a sulfated TiO_2 solid acid composite by a photodeposition method. The synthesized noble metal-modified $\text{SO}_4^{2-}/\text{M-TiO}_2$ ($\text{M} = \text{Ag}, \text{Au}, \text{Rh}, \text{and Pt}$) solid-acid catalysts were characterized by X-ray diffraction (XRD), Brunauer-Emmett-Teller (BET), transmission electron microscopy (TEM), X-ray photoelectron spectroscopy (XPS), Fourier transform infrared spectroscopy (FT-IR), electron spin resonance (ESR), and electrochemical impedance spectroscopy (EIS) analyses. The $\text{SO}_4^{2-}/\text{Au-TiO}_2$ catalyst showed the best catalytic activity for the synthesis of citric acid *n*-butyl acetate (CABu) in the esterification reaction of citric acid (CA) with *n*-butyl alcohol (*n*BuOH) and in the decomposition of methyl orange (MO). Among all the samples, the $\text{SO}_4^{2-}/\text{Au-TiO}_2$ catalyst showed the largest BET specific surface area, strongest intensity of surface-adsorbed sulfate groups in the FT-IR spectrum, highest transient photocurrent response, and smallest EIS radius in the photoelectric chemical test, and strongest signal intensities of the $\text{DMPO}\cdot\text{OH}$ and $\text{DMPO}\cdot\text{O}_2^-$ adducts in the ESR spectrum. The $\text{SO}_4^{2-}/\text{Au-TiO}_2$ catalyst was simultaneously used to esterification reactions and decomposition of organic dyes for industrial applications.

2. Experimental

2.1. Catalyst Preparation. All the chemicals including TiO_2 (pure anatase phase, 99% content, 15 nm, 170 m^2/g , Alfa Aesar) were of reagent grade and were used as received without any further purification.

The noble metal-loaded TiO_2 samples were prepared by the photodeposition method. The TiO_2 powder and a certain amount of noble metal salt were mixed in deionized water; a 300 W Xenon arc lamp (PLS-SXE 300, Beijing Perfectlight) was used as the light source. After irradiating for 5 h, the mixture was filtered, washed, and dried. Then, the resulting solid was filtered and washed twice with deionized water.

The sulfated TiO_2 was prepared by the ultrasonic method. In a typical synthesis, 1 g of TiO_2 powder was dissolved in 15 mL of 1 M H_2SO_4 , and the mixture was sonicated for 1 h. The solid products were collected after filtration, and then dried in an oven at 60 °C for 12 h, and finally calcined in air at 500 °C for 3 h.

The procedure for the preparation of sulfated $\text{SO}_4^{2-}/\text{M-TiO}_2$ ($\text{M} = \text{Ag}, \text{Au}, \text{Rh}, \text{and Pt}$) was the same as that for sulfated TiO_2 ; only TiO_2 was changed to M-TiO_2 .

2.2. Characterization of Catalysts. The phase composition of the samples and crystallite size were determined from their XRD patterns, which were obtained using an X'Pert X-ray diffractometer (PANalytical, Netherlands) using $\text{Cu K}\alpha$ radiation ($\lambda = 0.15406 \text{ nm}$) at a scan rate of $2^\circ/\text{min}$ from 20° to 90° (2θ). The accelerating voltage and applied current were 40 kV and 40 mA, respectively. The crystallite size was calculated from the X-ray line-broadening analysis using the Scherrer formula.

The BET surface areas of the samples were obtained from the N_2 adsorption/desorption isotherms determined at liquid nitrogen temperature (77 K) using an automatic analyzer ASAP 2010 (Micromeritics, China). The samples were degassed for 2 h under vacuum at 350 °C prior to adsorption. The equilibrium time for each point of the BET was 30 min.

The microstructures of the samples were determined by TEM and high-resolution TEM (HRTEM) images at an accelerating voltage of 200 kV using an EM 2010 EX instrument (Jeol, Japan). The samples were deposited on TiO_2 nanoparticles supported by copper grids from the ultrasonically processed ethanol solutions of the products.

The UV-vis diffuse reflection spectra (DRS) were recorded using a Varian Cary 500 Scan UV-vis-NIR spectrometer with BaSO_4 as the reference sample.

The XPS spectra were recorded using a VG ESCALAB 250 XPS system (Thermo Fisher Scientific, USA) using a monochromated $\text{Al K}\alpha$ X-ray source (15 kV, 200 W, 500 mm pass energy = 20 eV) and a charge neutralizer. All the binding energies were referenced to the C 1s peak at 284.6 eV of surface adventitious carbon.

The FT-IR spectra were recorded using a Nicolet 670 FT-IR spectrometer (Nicolet, USA). The samples were pressed using a KBr disk (18 mm diameter, 25–30 mg) preparation apparatus. The samples were dried at 250 °C for 2 h prior to pressing. The FT-IR spectra were recorded using a Nicolet 670 FT-IR spectrometer using a deuterated triglycine sulfate (DTGS) detector at a resolution of 4 cm^{-1} and for 32 scans.

The light/dark short-circuit photocurrent response was recorded using the Epsilon electrochemical workstation (BAS, USA) equipped with a Pt foil counter electrode and saturated calomel electrode (SCE) as the reference electrode. A size of $0.5 \times 0.5 \text{ cm}^2$ sample was coated on a fluorine-doped FTO glass as the working electrode. The three electrodes were immersed in a Na_2SO_4 electrolyte solution (0.5 M), and the working electrode was irradiated by a 365 nm light irradiation (Hamamatsu, LC8). The properties of the catalysts under AC polarization were evaluated by EIS experiments using a potentiostat (Zahner-IM6, Zahner, Germany).

The electron paramagnetic resonance (EPR) spectra were recorded using a Bruker A-300-EPR X-band spectrometer. The $\cdot\text{OH}$ radicals were detected in a dimethyl pyridine *N*-oxide (DMPO)/catalyst/water suspension, and the $\cdot\text{O}_2^-$ radicals in a DMPO/catalyst/methanol suspension (DMPO = 0.05 M, mass of samples = 3 mg, volume of solvent = 0.5 mL, and wavelength of excitation = 365 nm).

TABLE 1: Physicochemical characteristics of as-prepared samples.

Sample	Crystal size (nm) ^a	Pore volume (mL/g)	Pore size (nm)	SBET (m ² /g)
TiO ₂	15.40	0.38	9.04	168.69
SO ₄ ²⁻ /TiO ₂	15.92	0.38	17.10	190.03
SO ₄ ²⁻ /Ag-TiO ₂	15.90	0.40	16.98	193.26
SO ₄ ²⁻ /Au-TiO ₂	15.84	0.41	16.60	198.85
SO ₄ ²⁻ /Rh-TiO ₂	15.86	0.40	16.64	196.08
SO ₄ ²⁻ /Pt-TiO ₂	15.87	0.39	16.92	194.32

^aCalculated from the XRD results.

2.3. Catalytic Performance. The catalytic performance of the solid-acid samples was investigated by evaluating their catalytic activity in the esterification reaction of CA and *n*BuOH to synthesize CABu. The reaction was carried out in a well-stirred oil batch reactor and conducted in a liquid phase. A predetermined amount (12.6 g CA, 27.5 mL *n*BuOH, and 0.25 g catalyst) of the reagents was loaded into the reactor and heated to 400 K for 6 h. The liquid products were analyzed by gas chromatography (GC 7900, Techcomp, China) after each 30 min of the reaction.

The photocatalytic performances of the samples were evaluated from their activities in the decomposition of MO in an aqueous solution; a halogen lamp was used as the light source. Each of these catalysts (100 mg) was added to 100 mL of an aqueous MO solution (20 ppm) at room temperature. To achieve the adsorption-desorption equilibrium, the solution was continuously stirred for 30 min in the dark before the light was turned on. At a specific time interval (15 min) of irradiation, 2 mL aliquots were withdrawn and centrifuged to separate the catalysts. The degradation rate (*D*) of MO was calculated using the equation: $D = (A_0 - A)/A_0 \times 100\%$ (A_0 : initial absorbance; A : final absorbance), by measuring its absorbance at 664 nm using a BK UV-1600 UV-vis spectrometer (Biobase, China).

3. Results and Discussion

3.1. Crystalline Phases and Texture of Samples. The crystalline phases and texture of the samples were characterized by their XRD and N₂ adsorption. Figure 1(a) shows the XRD patterns of TiO₂ and SO₄²⁻/M-TiO₂ (M = Ag, Au, Rh, and Pt) nanoparticles. For all the samples, the peaks at $2\theta = 25.1^\circ$, 37.6° , 48.0° , 53.8° , 55.0° , and 62.7° can be attributed to the typical anatase phase of TiO₂ (JCPDS: 21-1272) [24]. The peaks at $2\theta = 27.4^\circ$, 36.1° , and 54.3° with a lower intensity can be attributed to the rutile crystal structure. The XRD patterns show that the loading of noble metal nanoparticles did not change the crystal structure of TiO₂. For Au-TiO₂, four additional peaks at $2\theta = 38.185^\circ$, 44.381° , 64.571° , and 77.566° were observed; they can be attributed to Au (JCPDS: 04-0784). This indicates that a small amount of Au was formed during the synthesis. Similarly, the corresponding peaks for noble metal-modified nanoparticles were observed corresponding to Ag (JCPDS: 65-2871), Rh (JCPDS: 05-0685), and Pt (JCPDS: 65-2868) in the Ag-TiO₂, Rh-TiO₂, and Pt-TiO₂ powders, respectively (Figure 1(b)).

The change in the physic-chemical properties of the samples was studied by N₂ adsorption-desorption at 77 K. Figure 2 shows the N₂-sorption isotherms (Figure 2(a)) and the corresponding pore-size distribution curves (Figure 2(b)) of TiO₂, SO₄²⁻/TiO₂, and SO₄²⁻/M-TiO₂ (M = Ag, Au, Rh and Pt); their pore sizes are shown in Table 1. It can be seen obviously that they exhibited the typical type-IV adsorption curves with an hysteresis loop between the partial pressure $P/P_0 = 0.45-1.0$, suggesting that TiO₂, SO₄²⁻/TiO₂ and SO₄²⁻/M-TiO₂ maintained the mesoporous structure of the TiO₂ support. The BET surface areas of pure TiO₂, SO₄²⁻/TiO₂, and SO₄²⁻/M-TiO₂ samples were 168.69 m²/g, 190.03 m²/g, and 193.26–198.85 m²/g, respectively. Although the pore sizes increased, the SO₄²⁻/TiO₂ and SO₄²⁻/M-TiO₂ samples still exhibited much higher BET surface areas than TiO₂, possibly because of the reservation of the porous structure inside the particles under supercritical conditions [25]. Even the S-modification further increased the crystal sizes, because the O atom in the O–Ti–O network was replaced with the S atom with a relatively large atomic radius [26]. The results show that all the samples modified with noble metals maintained the mesoporous structure of the TiO₂ support, and noble metal nanoparticles were well dispersed on the surface of TiO₂.

3.2. Morphologies of Samples. The TEM and HRTEM analyses showed the morphologies and distributions of noble metal-modified nanoparticles in the solid samples. The TEM and HRTEM images of TiO₂, SO₄²⁻/TiO₂ and SO₄²⁻/M-TiO₂ (M = Ag, Au, Rh, and Pt) are shown in Figures 3(a1)–3(f1) and 3(a2)–3(f2), respectively. Small noble metal nanoparticles homogeneously dispersed on the surface of a larger TiO₂ phase [27]. No obvious difference was observed in the morphology of these nanoparticles, indicating that the particle dispersion of noble metals cannot change the lattice spacing of TiO₂ (101). The lattice spacing at 0.234 nm, 0.232 nm, 0.232 nm, and 0.209 nm can be attributed to Ag (111), Au (111), Rh (111), and Pt (200), respectively. Au nanoparticles showed the best dispersion on the surface of TiO₂ among all the samples.

3.3. UV-Vis Diffuse Reflection Spectra (DRS). Figure 4 shows the DRS of TiO₂, SO₄²⁻/TiO₂, and SO₄²⁻/M-TiO₂ (M = Ag, Au, Rh, and Pt) samples. An optical absorption threshold was observed at 383 nm, corresponding to the band gap of TiO₂ at 3.2 eV. This value is consistent with the reported value of

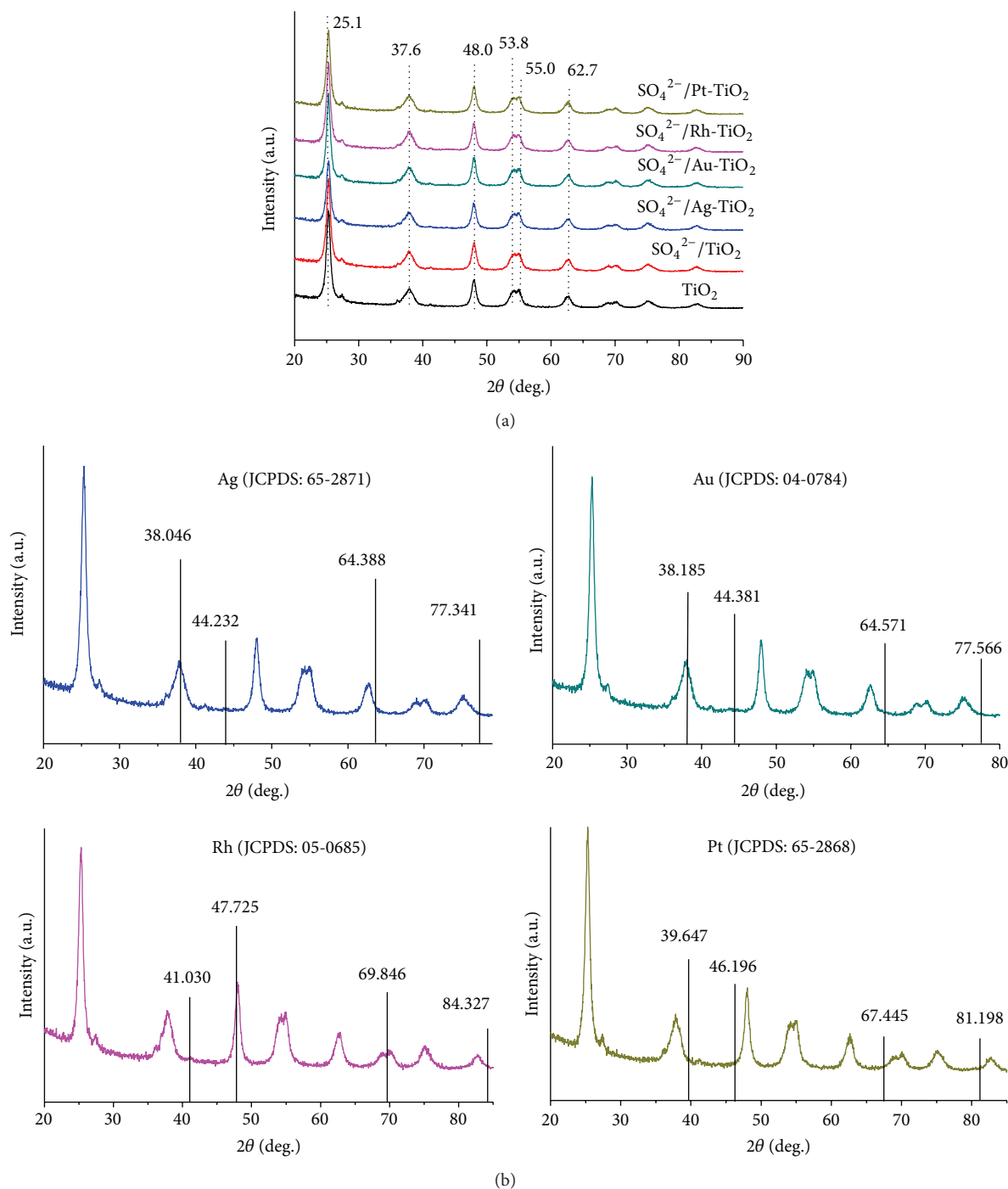


FIGURE 1: (a) XRD patterns of the samples (b) JCPDS of $\text{SO}_4^{2-}/\text{M-TiO}_2$ ($\text{M} = \text{Ag, Au, Rh, and Pt}$) samples.

anatase TiO_2 [28]. Compared to pure TiO_2 and $\text{SO}_4^{2-}/\text{TiO}_2$, the broad absorption bands of $\text{SO}_4^{2-}/\text{M-TiO}_2$ ($\text{M} = \text{Ag, Au, Rh, and Pt}$) can be attributed to the type of loaded noble metal nanoparticles. Clearly, a special strong absorption band was present in the range 450–650 nm for $\text{SO}_4^{2-}/\text{Au-TiO}_2$, corresponding to the located surface plasmon resonance of Au nanoparticles [29]. Therefore, the loading of noble metal nanoparticles into anatase $\text{SO}_4^{2-}/\text{TiO}_2$ may have contributed to the increased activities.

3.4. Surface Chemical States of the Samples. The chemical states of the samples were investigated by XPS. The C 1s peak of the aliphatic carbon with a binding energy (BE) of 284.6 eV was used as the reference. The spectra show no difference in the BEs of O and Ti atoms before and after the noble metal nanoparticles were dispersed homogeneously (Figure 5(a)). The O 1s, Ti 2p, and S 2p peaks of $\text{SO}_4^{2-}/\text{M-TiO}_2$ ($\text{M} = \text{Ag, Au, Rh, and Pt}$) are shown in Figure 5(b), confirming sulfation. The XPS spectra of Ag 3d, Au 4f, Rh 3d, and Pt

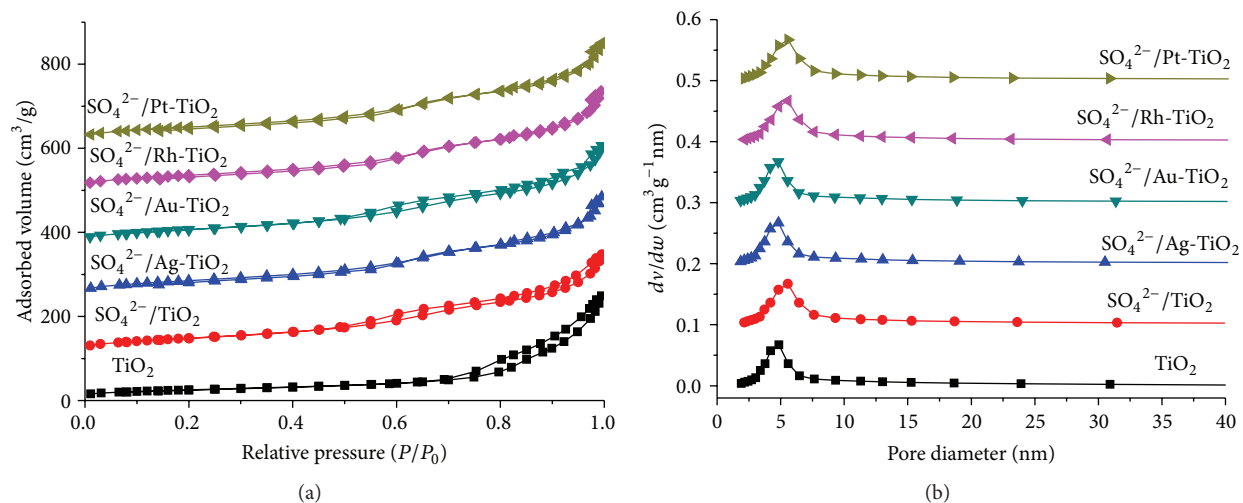


FIGURE 2: (a) N_2 -sorption isotherms and (b) corresponding pore-size distribution curves for the samples.

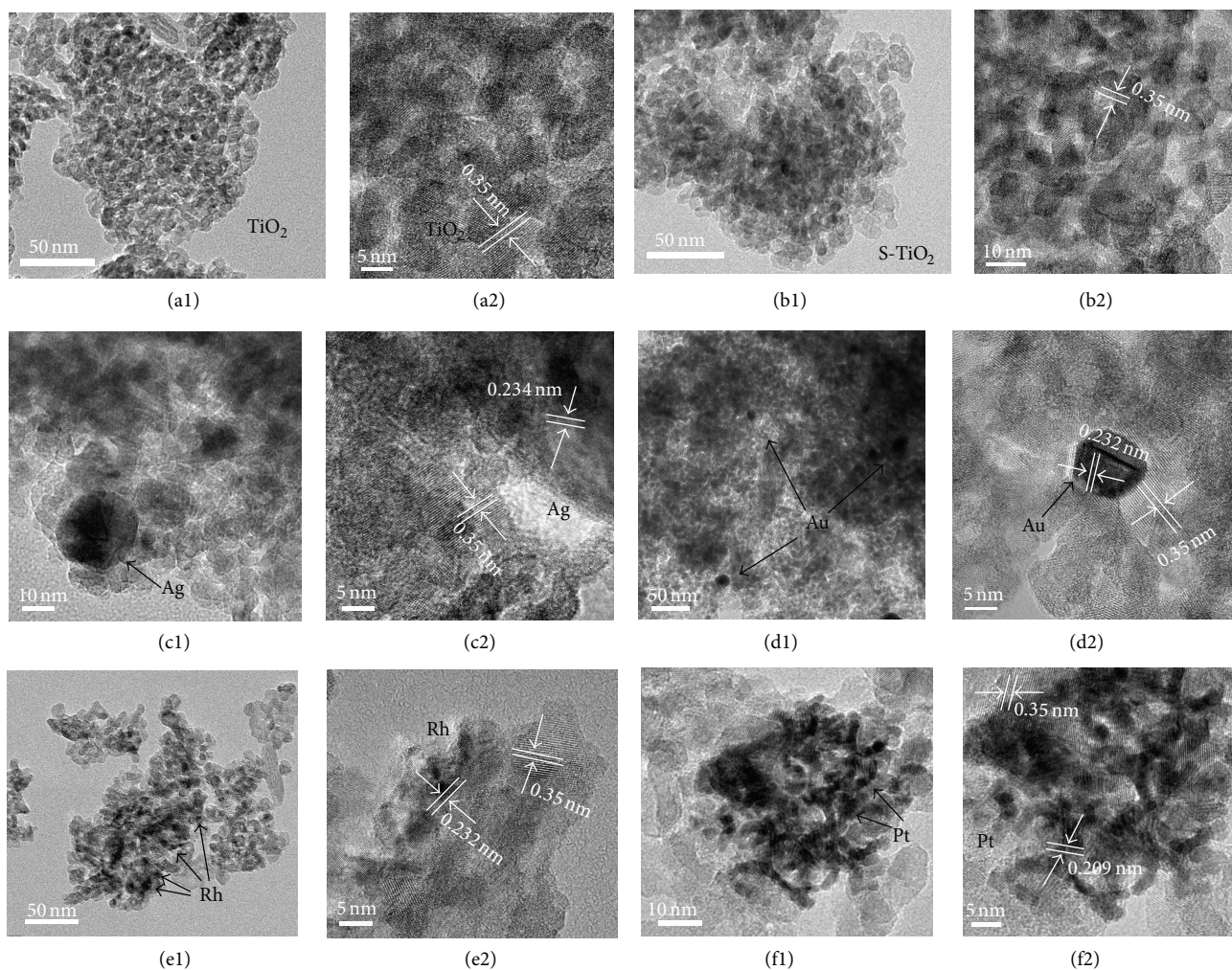


FIGURE 3: TEM and HRTEM images of TiO_2 (a1, a2), SO_4^{2-}/TiO_2 (b1, b2), $SO_4^{2-}/Ag-TiO_2$ (c1, c2), $SO_4^{2-}/Au-TiO_2$ (d1, d2), $SO_4^{2-}/Rh-TiO_2$ (e1, e2), and $SO_4^{2-}/Pt-TiO_2$ (f1, f2) samples.

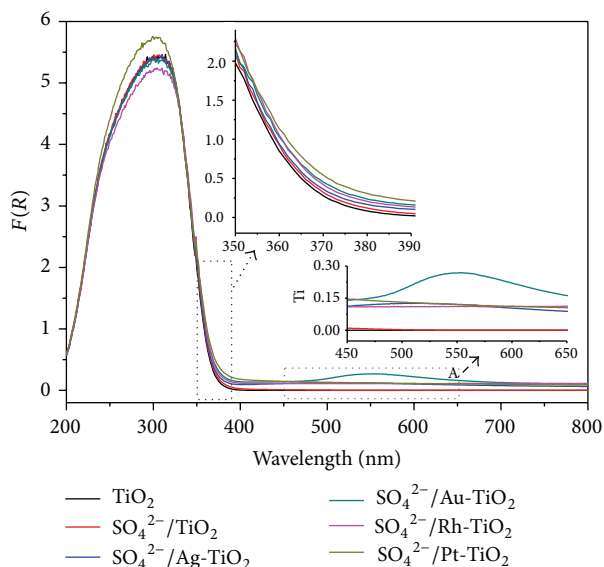


FIGURE 4: UV-vis DRS of the samples.

4f are shown in Figures 5(c)–5(f), respectively. The observed peaks at ca. 368 eV and 374 eV (Figure 5(c)) correspond to the $3d_{5/2}$ and $3d_{3/2}$ core levels of the Ag^0 cations in $\text{SO}_4^{2-}/\text{Ag-TiO}_2$; however, Ag^+ cations could not be identified because of the small differences in Bes [30]. The observed peaks at ca. 83.64 eV and 86.86 eV (Figure 5(d)) correspond to the $4f_{7/2}$ and $4f_{5/2}$ core levels of Au^0 cations in $\text{SO}_4^{2-}/\text{Au-TiO}_2$ [31]. The observed peaks at ca. 307.5 eV and 312.5 eV (Figure 5(e)) correspond to the $3d_{5/2}$ and $3d_{3/2}$ core levels of Rh^0 cations in $\text{SO}_4^{2-}/\text{Rh-TiO}_2$; the second pair of peaks with BEs of ~ 309.45 eV and 314.2 eV can be assigned to the $3d_{5/2}$ and $3d_{3/2}$ core levels of Rh^{3+} valence state, respectively [32]. The peaks at ca. 70.7 eV and 74.0 eV (Figure 5(f)) can be attributed to the $4f_{7/2}$ and $4f_{5/2}$ core levels of Pt^0 cations in $\text{SO}_4^{2-}/\text{Pt-TiO}_2$; the second pair of peaks with BEs of ~ 72.6 eV and 75.9 eV can be assigned to the $4f_{7/2}$ and $4f_{5/2}$ core levels of Pt^{2+} valence state, respectively [33].

Although the Au nanoparticle-loaded sulfated TiO_2 shows only the presence of Au^0 valence state, less than the BE of pure metallic Au, this is probably responsible for the improved catalytic activity. This indicates that the nanoparticles with Au^0 valence states are responsible for the catalytic activity in the esterification reaction to synthesize CABu and decomposition of MO.

3.5. FT-IR Spectra of Samples. The FT-IR spectra of TiO_2 , $\text{SO}_4^{2-}/\text{TiO}_2$, and $\text{SO}_4^{2-}/\text{M-TiO}_2$ ($\text{M} = \text{Ag}, \text{Au}, \text{Rh}, \text{and Pt}$) are shown in Figure 6 band was observed at 1105 cm^{-1} , corresponding to free SO_4^{2-} ; that is, free SO_4^{2-} groups is present in $\text{SO}_4^{2-}/\text{M-TiO}_2$. $\text{SO}_4^{2-}/\text{TiO}_2$ and $\text{SO}_4^{2-}/\text{M-TiO}_2$ showed two bands at 3422 cm^{-1} and 1637 cm^{-1} , in which one can be attributed to adsorbed water and the other can be attributed to the surface hydroxyl group of TiO_2 . The S–O stretching frequencies of $\text{SO}_4^{2-}/\text{TiO}_2$ and $\text{SO}_4^{2-}/\text{M-TiO}_2$ were found at

$1137\text{--}1128 \text{ cm}^{-1}$ and $1068\text{--}1051 \text{ cm}^{-1}$, respectively [34]. Based on the reported S–O stretching frequencies [35, 36], the two new absorption bands at 1133 cm^{-1} and 1062 cm^{-1} for $\text{SO}_4^{2-}/\text{M-TiO}_2$ and $\text{SO}_4^{2-}/\text{TiO}_2$ were the characteristics of chelating bidentate SO_4^{2-} group. Herein, the zero valence state of Au^0 may have changed the surface properties of the catalyst, consistent with the XPS data. The strongest intensity of both the 1133 cm^{-1} and 1062 cm^{-1} bands of the $\text{SO}_4^{2-}/\text{Au-TiO}_2$ can be attributed to the high concentration of surface-adsorbed sulfate groups.

3.6. Photoelectrochemical Properties and ESR Measurements of Samples. The photoelectronic chemical and ESR measurements of the samples were conducted. Figure 7 shows that the transient photocurrent responses of $\text{SO}_4^{2-}/\text{M-TiO}_2$ ($\text{M} = \text{Ag}, \text{Au}, \text{Rh}, \text{and Pt}$) were higher than those of $\text{SO}_4^{2-}/\text{TiO}_2$ and TiO_2 under 365 nm light irradiation (Hamamatsu Co., LC8). This is because the modification with noble metals can significantly enhance the photocurrent. This indicates a more efficient separation of the photoexcited charge carriers on catalysts under their radiation. $\text{SO}_4^{2-}/\text{Au-TiO}_2$ showed the highest transient photocurrent response (Figure 7(a)) and the smallest EIS radius (Figure 7(b)) in all the samples. This indicates that Au nanoparticles may have the best ability to decrease the impedance of electron transfer and increase the charge mobility. This is because of the optimized electronic band structure and interface/surface properties induced by the modification [37–39]. In the esterification reaction for CABu and decomposition of MO, the electron transfer efficiency and formation of active species induced by Au modification also play an important role.

$\cdot\text{OH}$ and $\cdot\text{O}_2^-$ radicals were detected by the DMPO spin-trapping EPR technique, contributing to a better understanding of the photoinduced hole and electrontransfer and photoredox processes as shown in Figures 8(a) and 8(b), respectively. Under the irradiation of $\lambda = 365 \text{ nm}$, four characteristic peaks of the ESR signal of $\text{DMPO}\cdot\text{OH}$ adduct were detected in all the aqueous suspensions of the samples (Figure 8(a)). Six characteristic peaks of the $\text{DMPO}\cdot\text{O}_2^-$ adduct were clearly observed in the ESR spectra (Figure 8(b)). The presence of the active species can be attributed to the reaction of photoinduced holes (h^+) with H_2O molecules [40, 41]. The signal intensities of the $\text{DMPO}\cdot\text{OH}$ and $\text{DMPO}\cdot\text{O}_2^-$ adducts in the ESR spectra of $\text{SO}_4^{2-}/\text{Au-TiO}_2$ were the strongest, indicating that this catalyst has the highest photocatalytic activity in the decomposition of MO. Thus, $\text{SO}_4^{2-}/\text{Au-TiO}_2$ catalyst may have increased the surface acidity for ester synthesis and dye decomposition, great practical value for industrial applications.

3.7. Acid Density Test. The total acid densities of all these catalysts were determined as follows: the samples (0.1 g) were placed in an Erlenmeyer flask and mixed with 15 mL of 2 mol/L NaCl solution. As H^+ ions were present in the SO_3H group of the sulfonated catalyst, they exchanged with Na^+ ions by ultrasonication for 60 min. After the filtration, a 0.02 mol/L NaOH solution was used to titrate the filtrate

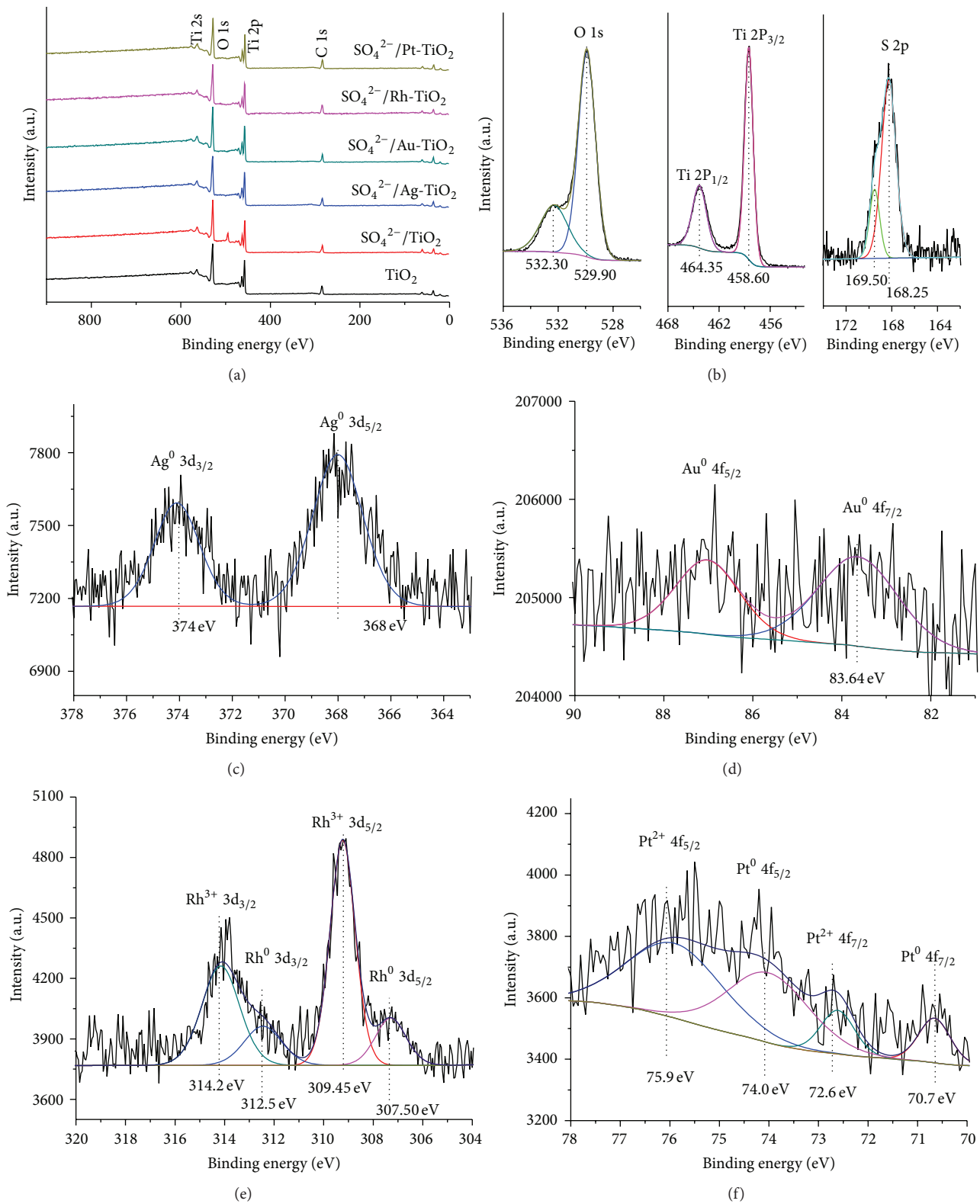


FIGURE 5: XPS (a) spectra of samples, (b) O 1s, Ti 2p, and S 2p peaks of $\text{SO}_4^{2-}/\text{M-TiO}_2$ samples, (c) Ag 3d spectra of $\text{SO}_4^{2-}/\text{Ag-TiO}_2$ sample, (d) Au 4f 3d spectra of $\text{SO}_4^{2-}/\text{Au-TiO}_2$ sample, (e) Rh 3d spectra of $\text{SO}_4^{2-}/\text{Rh-TiO}_2$ sample, and (f) Pt 4f spectra of $\text{SO}_4^{2-}/\text{Pt-TiO}_2$ sample.

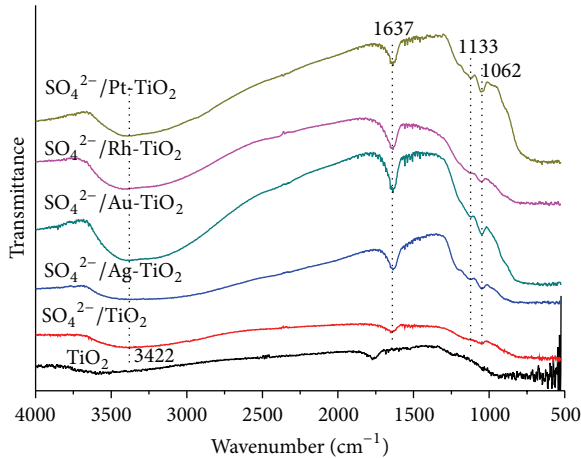


FIGURE 6: FT-IR spectra of samples.

using phenolphthalein as the indicator. When the color of the filtrate changed from colorless to slightly red, the endpoint of the titration reached [35]. The accurate acid quantity was calculated as follows:

$$c(\text{H}^+) = \frac{c(\text{OH}^-) \times \Delta V}{m}, \quad (1)$$

where $c(\text{H}^+)$ is the acid quantity of the sulfated samples; $c(\text{OH}^-)$ is the concentration of the NaOH solution; ΔV is the volume of the NaOH solution consumed in titration; and m is the quality of the samples used in ultrasonication.

The results of acid density are shown in Table 2. The amount of sulfate groups on TiO_2 was $201 \mu\text{mol/g}$ or $\sim 0.71 \text{ SO}_4^{2-}$ groups per nm^2 on the surface of TiO_2 . The surface coverage of SO_4^{2-} was calculated using the BET surface area. However, the amounts of SO_4^{2-} groups on M-TiO_2 ($\text{M} = \text{Ag, Au, Rh, and Pt}$) were $296 \mu\text{mol/g}$, $804 \mu\text{mol/g}$, $542 \mu\text{mol/g}$, $664 \mu\text{mol/g}$, or about 1.32, 2.71, 1.87, 2.05 SO_4^{2-} groups per nm^2 on the surface of TiO_2 , respectively. The surface sulfate groups played an important role in catalysis by offering active acid sites; evidently, the $\text{SO}_4^{2-}/\text{Au-TiO}_2$ had the most abundant Lewis acid sites with the highest acid density, increasing the catalytic activities.

3.8. Esterification Reactions for CABu on Samples. The catalytic activities of the $\text{SO}_4^{2-}/\text{TiO}_2$ and $\text{SO}_4^{2-}/\text{M-TiO}_2$ ($\text{M} = \text{Ag, Au, Rh, and Pt}$) samples were investigated using the CABu esterification reaction shown in Figure 11 as the model reaction, where the mass fraction of the catalyst was 2% of CA.

CABu can be widely used as a solvent in medical products, food packaging materials, and resin plasticizers [42]. Therefore, TiO_2 , $\text{SO}_4^{2-}/\text{TiO}_2$ and $\text{SO}_4^{2-}/\text{M-TiO}_2$ were used to test the performance of the catalysts in the esterification reaction of CA and $n\text{BuOH}$ to synthesize CABu. The results are shown in Figure 9.

Previously, 97.67% CABu conversion was attained at 393 K, with a reaction time of >270 min via the phosphotungstic acid loading of an epoxy resin catalyst [43]. In this

TABLE 2: Amount of SO_4^{2-} groups on prepared catalysts.

Samples	Amount ($\mu\text{mol/g}$)	SO_4^{2-} groups (per nm^2)
TiO_2	201	0.71
Ag-TiO_2 ($w(\text{Ag}) = 0.5\%$)	296	1.32
Au-TiO_2 ($w(\text{Au}) = 0.5\%$)	804	2.71
Rh-TiO_2 ($w(\text{Rh}) = 0.5\%$)	542	1.87
Pt-TiO_2 ($w(\text{Pt}) = 0.5\%$)	664	2.05

TABLE 3: CABu conversion of esterification reaction catalyzed by TiO_2 , $\text{SO}_4^{2-}/\text{TiO}_2$ and $\text{SO}_4^{2-}/\text{M-TiO}_2$ ($\text{M} = \text{Ag, Au, Rh, and Pt}$) solid-acid catalysts^a.

Samples	Conversion (%)
TiO_2	62.3
$\text{SO}_4^{2-}/\text{TiO}_2$	83.5
$\text{SO}_4^{2-}/\text{Ag-TiO}_2$ ($w(\text{Ag}) = 0.5\%$)	86.7
$\text{SO}_4^{2-}/\text{Au-TiO}_2$ ($w(\text{Au}) = 0.5\%$)	98.2
$\text{SO}_4^{2-}/\text{Rh-TiO}_2$ ($w(\text{Rh}) = 0.5\%$)	90.3
$\text{SO}_4^{2-}/\text{Pt-TiO}_2$ ($w(\text{Pt}) = 0.5\%$)	91.3

^a Reaction conditions: $T = 400 \text{ K}$, $P = 1 \text{ atm}$, and $T = 6 \text{ h}$.

study, a conversion rate of $>98.2\%$ was achieved at 400 K with $\text{SO}_4^{2-}/\text{Au-TiO}_2$ catalysts; the reaction time was almost the same as that of the previous report. Figure 9 shows the amount of CABu conversion in the esterification reaction using TiO_2 , $\text{SO}_4^{2-}/\text{TiO}_2$ and $\text{SO}_4^{2-}/\text{M-TiO}_2$ as the catalysts. The results show that all the sulfated samples had a better stability over 270 min, consistent with the reported esterification reactions as shown in Table 3. After the reactions reached equilibrium, $\text{SO}_4^{2-}/\text{Au-TiO}_2$ showed the highest catalytic activity for CABu at 400 K, whereas a blank experiment (with TiO_2 catalyst) showed that the conversion of CABu was $<63\%$. Notably, the sulfated TiO_2 catalysts clearly increased the catalytic activity for the esterification reaction to synthesize CABu; the loading of noble metals further increased the catalytic activity. Particularly, $\text{SO}_4^{2-}/\text{Au-TiO}_2$ exhibited the highest conversion rate; this can be attributed to the stronger acidity and the strong interactions between Au and $\text{SO}_4^{2-}/\text{TiO}_2$.

3.9. Photocatalytic Decomposition of MO. The photocatalytic activities of TiO_2 , $\text{SO}_4^{2-}/\text{TiO}_2$, and $\text{SO}_4^{2-}/\text{M-TiO}_2$ ($\text{M} = \text{Ag, Au, Rh, and Pt}$) samples were evaluated by using the photodecomposition of MO under halogen lamp irradiation. The results are shown in Figure 10. Noble metals had a high work function and formed a Schottky barrier between the semiconductor and metal; this trapped the injected electrons of the conduction band in TiO_2 and suppressed the recombination of photoelectrons and holes [44]. Moreover, $\text{SO}_4^{2-}/\text{Au-TiO}_2$ exhibited a much higher activity for the degradation rate than other noble metal-modified TiO_2 samples in the decomposition of MO. This is because Au nanoparticles not only increased the rate of electron-hole pair

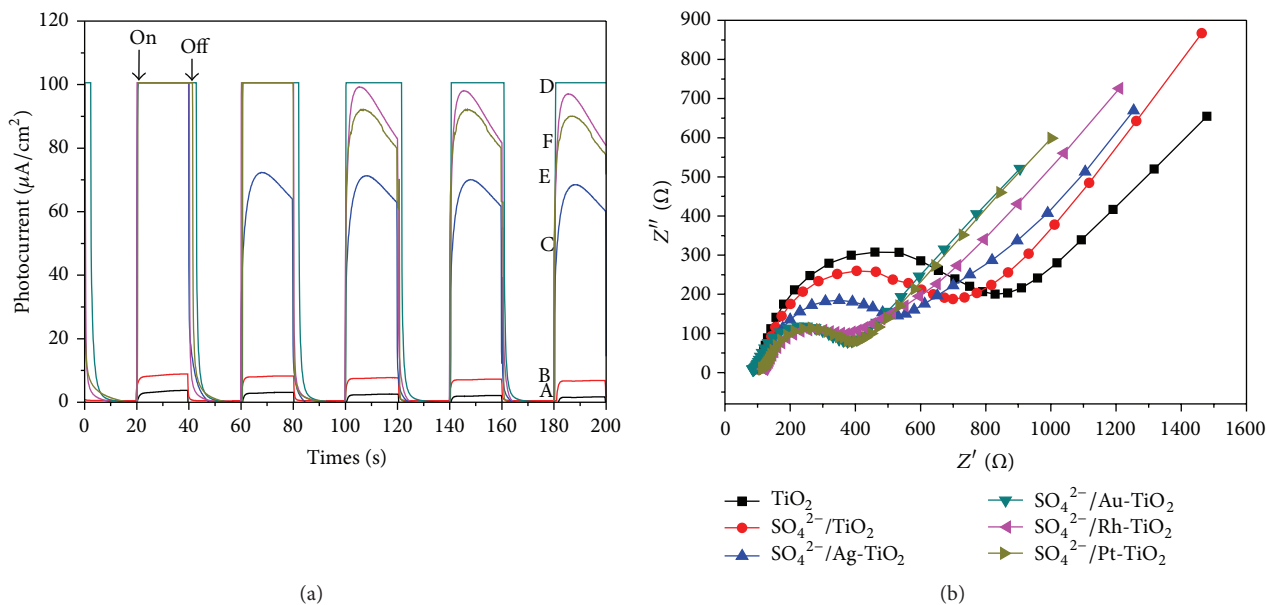


FIGURE 7: (a) Transient photocurrent response of (A) TiO_2 , (B) $\text{SO}_4^{2-}/\text{TiO}_2$, (C) $\text{SO}_4^{2-}/\text{Ag-TiO}_2$, (D) $\text{SO}_4^{2-}/\text{Au-TiO}_2$, (E) $\text{SO}_4^{2-}/\text{Rh-TiO}_2$, and (F) $\text{SO}_4^{2-}/\text{Pt-TiO}_2$ samples under intermittent UV light irradiation; (b) EIS of samples.

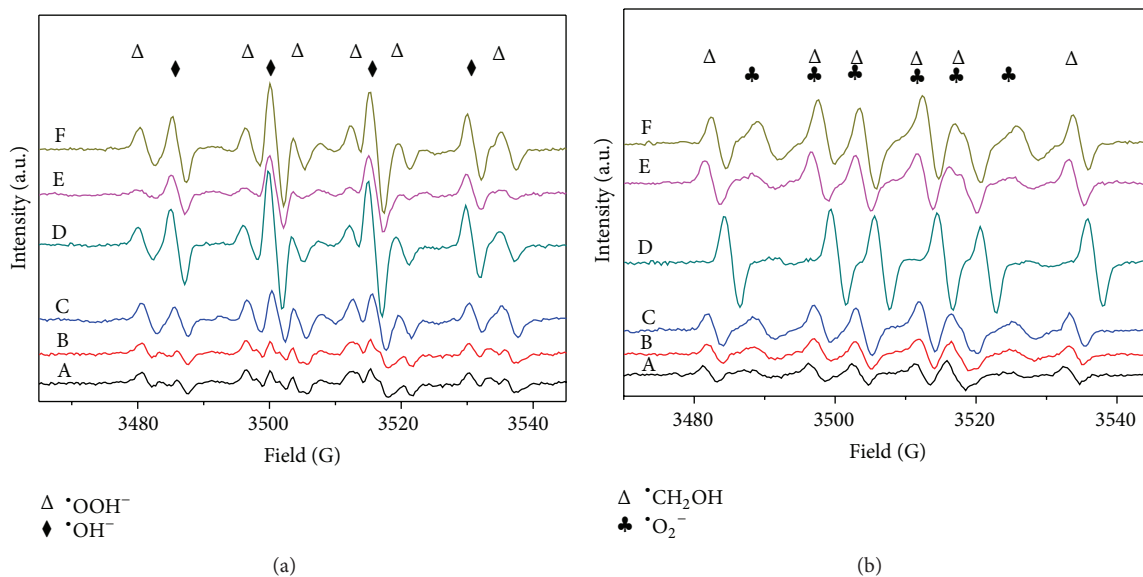


FIGURE 8: DMPO spin-trapping ESR spectra of (A) TiO_2 , (B) $\text{SO}_4^{2-}/\text{TiO}_2$, (C) $\text{SO}_4^{2-}/\text{Ag-TiO}_2$, (D) $\text{SO}_4^{2-}/\text{Au-TiO}_2$, (E) $\text{SO}_4^{2-}/\text{Rh-TiO}_2$, and (F) $\text{SO}_4^{2-}/\text{Pt-TiO}_2$ samples, at ambient temperature in an aqueous dispersion for (a) $\text{DMPO}\cdot\text{OH}$ and in a methanol dispersion for (b) $\text{DMPO}\cdot\text{O}_2^-$.

formation but also acted as a photosensitizer to harvest visible photons and converted them to electrical energy [45].

4. Conclusion

Noble metal-modified $\text{SO}_4^{2-}/\text{M-TiO}_2$ (M = Ag, Au, Rh, and Pt) catalysts were synthesized using the photodeposition and ultrasonic methods. The results show that $\text{SO}_4^{2-}/\text{Au-TiO}_2$

had the best catalytic activity in the esterification reactions of CA and *n*BuOH for the synthesis of CABu, and also in the decomposition of MO under halogen lamp irradiation. The enhanced activity can be attributed to stronger acidic sites, larger specific surface areas, and the composition or valence states of noble metal nanoparticles. Moreover, the photoelectrochemical and ESR measurements confirmed the highest electron transfer efficiency and formation of OH^-

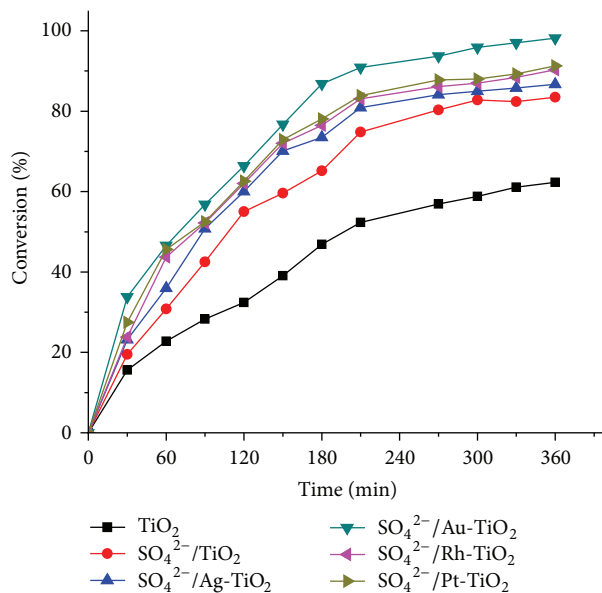


FIGURE 9: Conversion of CABu.

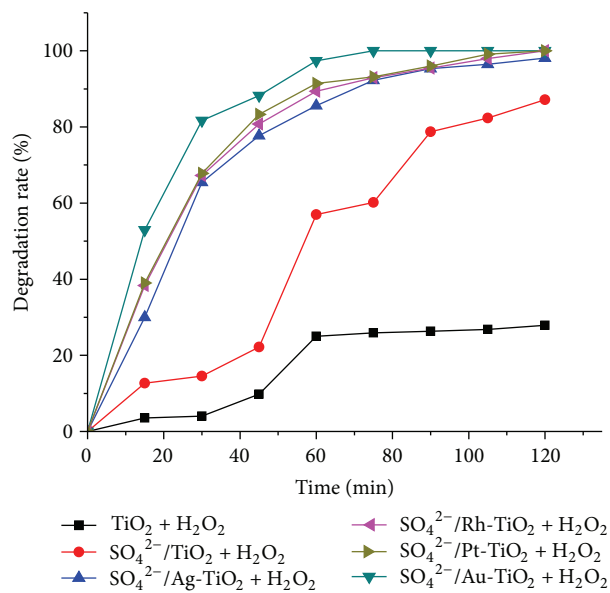


FIGURE 10: Photocatalytic decomposition of samples.

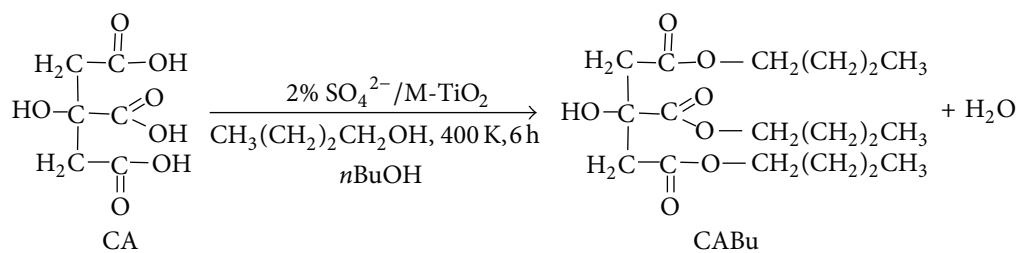


FIGURE 11

and $\cdot\text{O}_2^-$ active species in $\text{SO}_4^{2-}/\text{Au-TiO}_2$ sample. This study indicates a great potential of the solid-acid catalysts for esterification reactions and wastewater treatments.

Conflict of Interests

The authors declare that there is no conflict of interests regarding the publication of this paper.

Acknowledgments

This work was financially supported by the Collaborative Innovation Center of Clean Coal Gasification Technology (XK1403, XK1401), Natural Fund of Fujian Province (2015J01601), and Youth Fund of Fujian Province (JA14290, JA15475).

References

- [1] J. Zhang, Q. Xu, Z. Feng, M. Li, and C. Li, "Importance of the relationship between surface phases and photocatalytic activity of TiO_2 ," *Angewandte Chemie—International Edition*, vol. 47, no. 9, pp. 1766–1769, 2008.
- [2] C. Yu, D. Cai, K. Yang, J. C. Yu, Y. Zhou, and C. Fan, "Sol-gel derived S, I-codoped mesoporous TiO_2 photocatalyst with high visible-light photocatalytic activity," *Journal of Physics and Chemistry of Solids*, vol. 71, no. 9, pp. 1337–1343, 2010.
- [3] A. Fujishima, X. Zhang, and D. A. Tryk, " TiO_2 photocatalysis and related surface phenomena," *Surface Science Reports*, vol. 63, no. 12, pp. 515–582, 2008.
- [4] M. Zhang, C. Chen, W. Ma, and J. Zhao, "Visible-light-induced aerobic oxidation of alcohols in a coupled photocatalytic system of dye-sensitized TiO_2 and TEMPO," *Angewandte Chemie—International Edition*, vol. 47, no. 50, pp. 9730–9733, 2008.
- [5] M. Grätzel, "Dye-sensitized solar cells," *Journal of Photochemistry and Photobiology C: Photochemistry Reviews*, vol. 4, no. 2, pp. 145–153, 2003.
- [6] X.-Q. Gong, A. Selloni, O. Dulub, P. Jacobson, and U. Diebold, "Small Au and Pt clusters at the anatase $\text{TiO}_2(101)$ surface: behavior at terraces, steps, and surface oxygen vacancies," *Journal of the American Chemical Society*, vol. 130, no. 1, pp. 370–381, 2008.
- [7] G. Liu, Y. Zhao, C. Sun, F. Li, G. Q. Lu, and H.-M. Cheng, "Synergistic effects of B/N doping on the visible-light photocatalytic activity of mesoporous TiO_2 ," *Angewandte Chemie—International Edition*, vol. 47, no. 24, pp. 4516–4520, 2008.
- [8] C. Yu and C. Y. Jimmy, "A simple way to prepare C–N-codoped TiO_2 photocatalyst with visible-light activity," *Catalysis Letters*, vol. 129, no. 3-4, pp. 462–470, 2009.
- [9] X. Chen, X. Wang, Y. Hou, J. Huang, L. Wu, and X. Fu, "The effect of postnitridation annealing on the surface property and photocatalytic performance of N-doped TiO_2 under visible light irradiation," *Journal of Catalysis*, vol. 255, no. 1, pp. 59–67, 2008.
- [10] C. Yu, J. C. Yu, and M. Chan, "Sonochemical fabrication of fluorinated mesoporous titanium dioxide microspheres," *Journal of Solid State Chemistry*, vol. 182, no. 5, pp. 1061–1069, 2009.
- [11] P. Periyat, S. C. Pillai, D. E. McCormack, J. Colreavy, and S. J. Hinder, "Improved high-temperature stability and sun-light-driven photocatalytic activity of sulfur-doped anatase TiO_2 ," *Journal of Physical Chemistry C*, vol. 112, no. 20, pp. 7644–7652, 2008.
- [12] D. S. Muggli and L. Ding, "Photocatalytic performance of sulfated TiO_2 and Degussa P-25 TiO_2 during oxidation of organics," *Applied Catalysis B: Environmental*, vol. 32, no. 3, pp. 181–194, 2001.
- [13] S. Liu, J.-H. Yang, and J.-H. Choy, "Microporous SiO_2 - TiO_2 nanosols pillared montmorillonite for photocatalytic decomposition of methyl orange," *Journal of Photochemistry and Photobiology A: Chemistry*, vol. 179, no. 1-2, pp. 75–80, 2006.
- [14] C. Chen, W. Ma, and J. Zhao, "Semiconductor-mediated photodegradation of pollutants under visible-light irradiation," *Chemical Society Reviews*, vol. 39, no. 11, pp. 4206–4219, 2010.
- [15] B. Krishnakumar and M. Swaminathan, "A recyclable and highly effective sulfated TiO_2 -P25 for the synthesis of quinoxaline and dipyrrophenazine derivatives at room temperature," *Journal of Organometallic Chemistry*, vol. 695, no. 24, pp. 2572–2577, 2010.
- [16] J. L. Roper-Vega, A. Aldana-Pérez, R. Gómez, and M. E. Niño-Gómez, "Sulfated titania [$\text{TiO}_2/\text{SO}_4^{2-}$]: a very active solid acid catalyst for the esterification of free fatty acids with ethanol," *Applied Catalysis A: General*, vol. 379, no. 1-2, pp. 24–29, 2010.
- [17] D. Yang, J. Li, M. Wen, and C. Song, "Selective catalytic reduction of NO_x with CH_4 over the in/sulfated TiO_2 catalyst," *Catalysis Letters*, vol. 122, no. 1-2, pp. 138–143, 2008.
- [18] B. Wang, X. Cui, H. Ma, and J. Li, "Photocatalytic activity of $\text{SO}_4^{2-}/\text{SnO}_2$ - TiO_2 catalysts: direct oxidation of n-heptane to ester under mild conditions," *Energy & Fuels*, vol. 21, no. 6, pp. 3748–3749, 2007.
- [19] S. Han, G. Zhang, H. Xi, D. Xu, X. Fu, and X. Wang, "Sulfated TiO_2 decontaminate 2-CEES and DMMP in vapor phase," *Catalysis Letters*, vol. 122, no. 1-2, pp. 106–110, 2008.
- [20] P. Chen, M. Du, H. Lei et al., " $\text{SO}_4^{2-}/\text{ZrO}_2$ -titania nanotubes as efficient solid superacid catalysts for selective mononitration of toluene," *Catalysis Communications*, vol. 18, pp. 47–50, 2012.
- [21] L. Liu, G. Zhang, L. Wang, T. Huang, and L. Qin, "Highly active S-modified ZnFe_2O_4 heterogeneous catalyst and its photo-Fenton behavior under UV-visible irradiation," *Industrial and Engineering Chemistry Research*, vol. 50, no. 12, pp. 7219–7227, 2011.
- [22] S. J. Wind, J. Appenzeller, R. Martel, V. Derycke, and P. Avouris, "Vertical scaling of carbon nanotube field-effect transistors using top gate electrodes," *Applied Physics Letters*, vol. 80, no. 20, pp. 3817–3819, 2002.
- [23] H. Nishikiori, M. Hayashibe, and T. Fujii, "Visible light-photocatalytic activity of sulfate-doped titanium dioxide prepared by the sol-gel method," *Catalysts*, vol. 3, no. 2, pp. 363–377, 2013.
- [24] S. M. Jung and P. Grange, "Characterization and reactivity of pure TiO_2 - SO_4^{2-} SCR catalyst: influence of SO_4^{2-} content," *Catalysis Today*, vol. 59, no. 3, pp. 305–312, 2000.
- [25] X. P. Lin, D. M. Song, X. Q. Gu, Y. L. Zhao, and Y. H. Qiang, "Synthesis of hollow spherical TiO_2 for dye-sensitized solar cells with enhanced performance," *Applied Surface Science*, vol. 263, pp. 816–820, 2012.
- [26] H. Li, X. Zhang, Y. Huo, and J. Zhu, "Supercritical preparation of a highly active S-doped TiO_2 photocatalyst for methylene blue mineralization," *Environmental Science & Technology*, vol. 41, no. 12, pp. 4410–4414, 2007.
- [27] I. Lee, J. B. Joo, Y. Yin, and F. Zaera, "A yolk@shell nanoarchitecture for Au/ TiO_2 catalysts," *Angewandte Chemie—International Edition*, vol. 50, no. 43, pp. 10208–10211, 2011.

- [28] J. R. Sohn and D. G. Lee, "Characterization of zirconium sulfate supported on TiO_2 and activity for acid catalysis," *Korean Journal of Chemical Engineering*, vol. 20, no. 6, pp. 1030–1036, 2003.
- [29] K. Yang, K. Huang, Z. He, X. Chen, X. Fu, and W. Dai, "Promoted effect of PANI as electron transfer promoter on CO oxidation over Au/TiO_2 ," *Applied Catalysis B: Environmental*, vol. 158–159, pp. 250–257, 2014.
- [30] C. Yu, L. Wei, X. Li, J. Chen, Q. Fan, and J. C. Yu, "Synthesis and characterization of Ag/TiO_2 -B nanosquares with high photocatalytic activity under visible light irradiation," *Materials Science and Engineering B: Solid-State Materials for Advanced Technology*, vol. 178, no. 6, pp. 344–348, 2013.
- [31] N. Kruse and S. Chenakin, "XPS characterization of Au/TiO_2 catalysts: binding energy assessment and irradiation effects," *Applied Catalysis A: General*, vol. 391, no. 1, pp. 367–376, 2011.
- [32] Y. V. Larichev, O. V. Netskina, O. V. Komova, and V. I. Simagina, "Comparative XPS study of $\text{Rh/Al}_2\text{O}_3$ and Rh/TiO_2 as catalysts for NaBH_4 hydrolysis," *International Journal of Hydrogen Energy*, vol. 35, no. 13, pp. 6501–6507, 2010.
- [33] T. Huizinga, H. v. T. Blik, J. Vis et al., "XPS investigations of Pt and Rh supported on $\gamma\text{-Al}_2\text{O}_3$ and TiO_2 ," *Surface Science*, vol. 135, no. 1, pp. 580–596, 1983.
- [34] Y.-H. Xu, L.-Y. Wang, Q. Zhang, S.-J. Zheng, X.-J. Li, and C. Huang, "Correlation between photoreactivity and photo-physics of sulfated TiO_2 photocatalyst," *Materials Chemistry and Physics*, vol. 92, no. 2–3, pp. 470–474, 2005.
- [35] T. Yamaguchi, "Recent progress in solid superacid," *Applied Catalysis*, vol. 61, no. 1, pp. 1–25, 1990.
- [36] Y. M. Wang, C. Z. Chen, J. H. Luo et al., "Studies on the acidity, structures and crystalline phases of $\text{SO}_4^{2-}/\text{TiO}_2$, $\text{PO}_4^{3-}/\text{TiO}_2$, $\text{BO}_3^{3-}/\text{TiO}_2$ solid acids," *Chinese Journal of Structural Chemistry*, vol. 18, no. 3, pp. 175–181, 1999.
- [37] G. Zhang, M. Zhang, X. Ye, X. Qiu, S. Lin, and X. Wang, "Iodine modified carbon nitride semiconductors as visible light photocatalysts for hydrogen evolution," *Advanced Materials*, vol. 26, no. 5, pp. 805–809, 2014.
- [38] N. Zhang, M.-Q. Yang, Z.-R. Tang, and Y.-J. Xu, "CdS-graphene nanocomposites as visible light photocatalyst for redox reactions in water: a green route for selective transformation and environmental remediation," *Journal of Catalysis*, vol. 303, pp. 60–69, 2013.
- [39] G. Zhang and X. Wang, "A facile synthesis of covalent carbon nitride photocatalysts by Co-polymerization of urea and phenylurea for hydrogen evolution," *Journal of Catalysis*, vol. 307, pp. 246–253, 2013.
- [40] W. Wu, L. Wen, L. Shen, R. Liang, R. Yuan, and L. Wu, "A new insight into the photocatalytic reduction of 4-nitroaniline to p-phenylenediamine in the presence of alcohols," *Applied Catalysis B: Environmental*, vol. 130–131, pp. 163–167, 2013.
- [41] W. Adam, M. A. Arnold, M. Grüne, W. M. Nau, U. Pischel, and C. R. Saha-Möller, "Spiroiminodihydantoin is a major product in the photooxidation of 2'-deoxyguanosine by the triplet states and oxyl radicals generated from hydroxyacetophenone photolysis and dioxetane thermolysis," *Organic Letters*, vol. 4, no. 4, pp. 537–540, 2002.
- [42] J. Xu, J. Jiang, L. V. Wei, and Y. Gao, "Synthesis of tributyl citrate using solid acid as a catalyst," *Chemical Engineering Communications*, vol. 198, no. 4, pp. 474–482, 2010.
- [43] Y. Huang, J. Guo, N. Yu et al., "Preparation and catalytic performance of $\text{PW}_{12}/\text{E-12}$ over esterification reaction of citric acid with n-Butyl alcohol," *Speciality Petrochemicals*, vol. 32, no. 4, pp. 6–10, 2015.
- [44] V. Subramanian, E. E. Wolf, and P. V. Kamat, "Catalysis with TiO_2 /gold nanocomposites. Effect of metal particle size on the Fermi level equilibration," *Journal of the American Chemical Society*, vol. 126, no. 15, pp. 4943–4950, 2004.
- [45] J. Long, H. Chang, Q. Gu et al., "Gold-plasmon enhanced solar-to-hydrogen conversion on the 001 facets of anatase TiO_2 nanosheets," *Energy & Environmental Science*, vol. 7, no. 3, pp. 973–977, 2014.

